SINTEF
PROCEEDINGS
2

Proceedings of the 12th International Conference on Computational Fluid Dynamics in the Oil & Gas, Metallurgical and Process Industries

Progress in Applied CFD – CFD2017

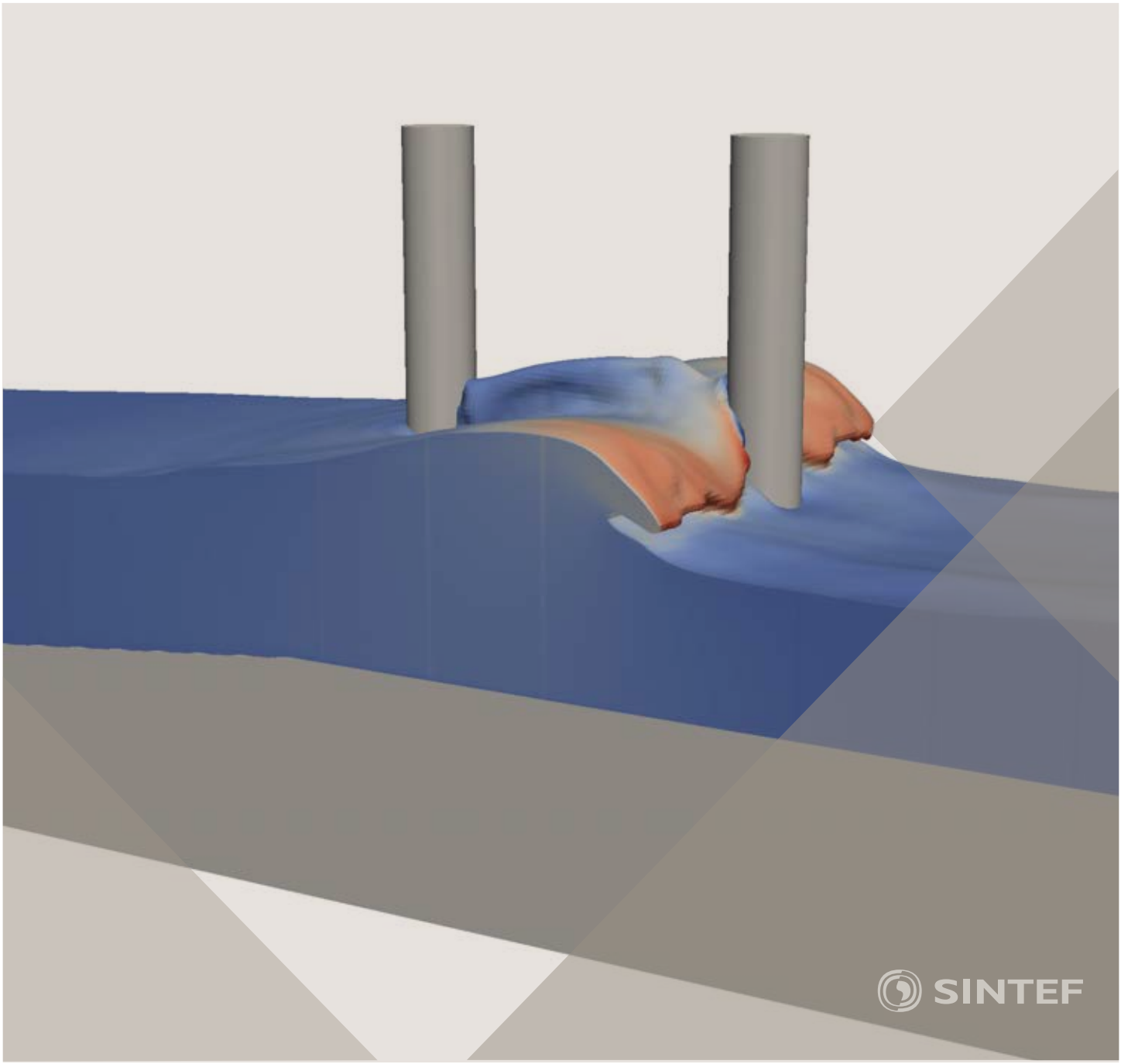

SINTEF Proceedings

Editors:
Jan Erik Olsen and Stein Tore Johansen

Progress in Applied CFD – CFD2017

Proceedings of the 12th International Conference on Computational Fluid Dynamics in the Oil & Gas, Metallurgical and Process Industries

SINTEF Academic Press

SINTEF Proceedings no 2
Editors: Jan Erik Olsen and Stein Tore Johansen
Progress in Applied CFD – CFD2017
Selected papers from 10th International Conference on Computational Fluid Dynamics in the Oil & Gas, Metallurgical and Process Industries

Key words:
CFD, Flow, Modelling

Cover, illustration: Arun Kamath

ISSN 2387-4295 (online)
ISBN 978-82-536-1544-8 (pdf)

© Copyright SINTEF Academic Press 2017
The material in this publication is covered by the provisions of the Norwegian Copyright Act. Without any special agreement with SINTEF Academic Press, any copying and making available of the material is only allowed to the extent that this is permitted by law or allowed through an agreement with Kopinor, the Reproduction Rights Organisation for Norway. Any use contrary to legislation or an agreement may lead to a liability for damages and confiscation, and may be punished by fines or imprisonment

SINTEF Academic Press
Address: Forskningsveien 3 B
PO Box 124 Blindern
N-0314 OSLO
Tel: +47 73 59 30 00
Fax: +47 22 96 55 08

www.sintef.no/byggforsk
www.sintefbok.no

SINTEF Proceedings
SINTEF Proceedings is a serial publication for peer-reviewed conference proceedings on a variety of scientific topics.
The processes of peer-reviewing of papers published in SINTEF Proceedings are administered by the conference organizers and proceedings editors. Detailed procedures will vary according to custom and practice in each scientific community.

PREFACE

This book contains all manuscripts approved by the reviewers and the organizing committee of the 12th International Conference on Computational Fluid Dynamics in the Oil & Gas, Metallurgical and Process Industries. The conference was hosted by SINTEF in Trondheim in May/June 2017 and is also known as CFD2017 for short. The conference series was initiated by CSIRO and Phil Schwarz in 1997. So far the conference has been alternating between CSIRO in Melbourne and SINTEF in Trondheim. The conferences focuses on the application of CFD in the oil and gas industries, metal production, mineral processing, power generation, chemicals and other process industries. In addition pragmatic modelling concepts and bio-mechanical applications have become an important part of the conference. The papers in this book demonstrate the current progress in applied CFD.

The conference papers undergo a review process involving two experts. Only papers accepted by the reviewers are included in the proceedings. 108 contributions were presented at the conference together with six keynote presentations. A majority of these contributions are presented by their manuscript in this collection (a few were granted to present without an accompanying manuscript).

The organizing committee would like to thank everyone who has helped with review of manuscripts, all those who helped to promote the conference and all authors who have submitted scientific contributions. We are also grateful for the support from the conference sponsors: ANSYS, SFI Metal Production and NanoSim.

Stein Tore Johansen & Jan Erik Olsen

Organizing committee:

Conference chairman: Prof. Stein Tore Johansen
Conference coordinator: Dr. Jan Erik Olsen
Dr. Bernhard Müller
Dr.Sigrid Karstad Dahl
Dr.Shahriar Amini
Dr.Ernst Meese
Dr.Josip Zoric
Dr.Jannike Solsvik
Dr.Peter Witt

Scientific committee:

Stein Tore Johansen, SINTEF/NTNU
Bernhard Müller, NTNU
Phil Schwarz, CSIRO
Akio Tomiyama, Kobe University
Hans Kuipers, Eindhoven University of Technology
Jinghai Li, Chinese Academy of Science
Markus Braun, Ansys
Simon Lo, CD-adapco
Patrick Segers, Universiteit Gent
Jiyuan Tu, RMIT
Jos Derksen, University of Aberdeen
Dmitry Eskin, Schlumberger-Doll Research
Pär Jönsson, KTH
Stefan Pirker, Johannes Kepler University
Josip Zoric, SINTEF

CONTENTS

EFFECT OF LIFT FORCE ON DENSE GAS-FLUIDIZED BEDS OF NON-SPHERICAL PARTICLES

Ivan MEMA[1]*, **Vinay V. MAHAJAN**[1], **Barry W. FITZGERALD**[1], **Hans KUIPERS**[2], **Johan T. PADDING**[1]

[1]Delft University of Technology, Process & Energy Department, Intensified Reaction & Separation Systems,Leeghwaterstraat 39, 2628 CB Delft, The Netherlands

[2]Department of Chemical Engineering and Chemistry, Multiphase Reactors Group, Eindhoven University of Technology, 5600 MB Eindhoven, The Netherlands

* E-mail: i.mema@tudelft.nl

ABSTRACT

In industry we encounter many processes that rely on equipment in which particles are suspended by a gas flow, such as pneumatic conveyors, CFB gasifiers, combustors and fluidized bed reactors. In numerical models of these processes, particles have traditionally been represented as spheres, thus limiting complexities associated with drag or lift forces. However, spherical particles are not representative of the entities encountered in real systems. For example, non-spherical biomass particles of varying aspect ratios are used in the production of biomass fuels.

Thus far literature is quite limited when it comes to hydrodynamic forces experienced by non-spherical particles under fluidized conditions. In fluidized beds, particles will experience varying lift force conditions dependent on the orientation of the particle relative to the direction of the flow. In this study, we investigate numerically the effect of different lift force coefficient correlations on fluidization of spherocylindrical particles. We employ correlations derived from previous simulations on non-spherical particles and aerofoil dynamics in simulations. We also look into the effect of the Di Felice approximation, in this case applied to take into account the effect of surrounding particles on the lift force. Particle interactions are modelled using the Open Source engine CFDEM, which uses the OpenFOAM computational fluid dynamics (CFD) solver to describe the fluid component and LIGGGHTS to implement discrete element method (DEM) calculations. We investigate the importance of lift forces on non-spherical particles under dense fluidised conditions and compare results to the case of spherical particles where lift forces are often neglected.

Keywords: Fluidized bed, granular flow, CFD-DEM, non-spherical particle, lift force.

NOMENCLATURE

DEM - Spherocylinder particles

$\mathbf{v}_i$	Particle velocity, $[m/s]$.
m_i	Mass, $[kg]$.
ρ_p	Density, $[kg/m^3]$.
$\boldsymbol{\omega}_i$	Angular velocity, $[rad/s]$.
$\mathbf{I}_i$	Moment of inertia, $[kg/m^2]$.
P_i	Identification for the i^{th} particle, $[-]$.
$\mathbf{r}_i$	Position of centre of mass, $[m]$.
L	Shaft length, $[m]$.
R	Characteristic radius, $[m]$.
$\mathbf{u}_i$	Orientation unit vector, $[-]$.
k_n	Normal spring constant, $[N/m]$.
η_n	Normal damping coefficient, $[kg/s]$.
$\mathbf{n}_{12}$	Normal unit vector, $[-]$.
$\mathbf{t}_{12}$	Tangential unit vector, $[-]$.
k_t	Tangential spring constant, $[N/m]$.
η_t	Tangential damping coefficient, $[kg/s]$.

CFD - Fluid

ε_f	volume fraction, $[-]$.
ρ_f	Density, $[kg/m^3]$.
$\mathbf{v}_f$	Fluid velocity, $[m/s]$.
C_D	Drag coefficient $[-]$.
$\mathbf{F}_D$	Drag force $[N]$.
Re_p	Reynolds number of particle in fluid $[-]$.
C_L	Lift coefficient $[-]$.
$\mathbf{F}_L$	Lift force $[N]$.
U_{mf}	Minimum fluidization velocity $[m/s]$.

INTRODUCTION

Many industrial processes such as fluidized bed reactors, cyclone separators, dust collectors and pulverized-coal combustors involve particle-laden in gas flows. These devices are categorized as gas-solid contactors, of which the fluidized bed reactor is a proto-typical example (Werther, 2000; Warnecke, 2000; Grace *et al.*, 1997). Due to their favourable mass and heat transfer characteristics, gas-fluidized beds are employed in many branches of industry such as the chemical (Son and Kim, 2006), petrochemical (Williams and Williams, 1999) and energy industries (Nikoo and Mahinpey, 2008). In addition, fluidized bed reactors are used in large-scale operations involving the granulation, drying and synthesis of fuels, base chemicals and polymers (Grace *et al.*, 1997). In recent years there has been increased application of fluidized beds in biomass energy production (McKendry, 2002; Bridgwater, 2003, 2006; Alauddin *et al.*, 2010). Therefore predicting the response of dense gas-solid flows in fluidized reactors via computational investigation is crucial for both reactor design and determination of optimal operating conditions. However simulations of dense gas-solid flows generally represent the solid phase as perfect spherical entities whereas, in reality, the solid phase is composed of particles of varying geometry. For example, in biomass energy production, biomass particles are usually non-spherical (Kruggel-Emden and Vollmari, 2016; Gil *et al.*, 2014).

With regards to implementation, describing non-spherical particles in simulations gives rise to a number of issues. While spheres can be described by a single parameter, i.e. diameter, non-spherical particles require more parameters. Even regular non-spherical shapes, such as ellipsoids and spherocylinders, require at least two parameters. When the particles become significantly irregular, it becomes computationally more demanding to detect particle-particle interactions and subsequently calculate the resulting contact force.

An additional concern is the determination of the hydrodynamic forces and torques on particles due to interaction with the fluid flow. For non-spherical particles, both the hydrodynamic forces, such as drag and transverse lift, and pitching and rotational torque can vary appreciably with particle orientation and thus crucially dictate the translational motion of the particles. Drag force, lift force and torques are characterised by dimensionless coefficients that depend on particle velocity and orientation relative to the flow and Reynolds number (Re). A number of drag force coefficients for a variety of non-spherical particles have been formulated (Tran-Cong *et al.*, 2004; Loth, 2008; Hölzer and Sommerfeld, 2008, 2009) while, recently, lift coefficient correlations have also been derived for non-spherical particles (Zastawny *et al.*, 2012; Richter and Nikrityuk, 2013; Ouchene *et al.*, 2015, 2016).

In the case of a dilute suspension, depending on the Reynolds number, the lift force can be more than half the drag force for non-spherical particles in a gas flow and, as a result, significantly influence the trajectory of non-spherical particles (Richter and Nikrityuk, 2013). However, it is not clear what effect lift force will have on non-spherical particles in dense systems such as those encountered in dense gas-fluidized systems. In this study we will investigate numerically the effect of differing lift force expressions and coefficients on non-spherical particles, specifically spherocylindrical particles, in a laboratory scale gas-fluidized bed reactor. We will employ lift force correlations derived from previous studies on non-spherical particles (Zastawny *et al.*, 2012) and from aerofoil dynamics (Hoerner, 1965). Particle interactions are numerically described using the Open Source engine CFDEM, which combines the OpenFOAM computational fluid dynamics (CFD) solver to describe the fluid component with the LIGGGHTS software package to implement discrete element method (DEM) calculations (Mahajan *et al.*, 2017). We present results on the importance of lift forces on non-spherical particles by studying the evolution of void fraction, particle velocity and particle alignment in the reactor.

This paper is arranged as follows. We will first outline the CFD-DEM numerical model used in this study focusing on the implemetation of contact detection, drag forces and lift forces for spherocylindrical particles. In the results section we will explore the effect of differing lift force expressions on particle dynamics in dense fluidized beds. Specifically we will focus on the variation of particle velocity along the direction of fluid flow, the evolution of voidage conditions in the reactor and particle alignment. Finally we will draw conclusions from this study and provide an outlook for future studies.

NUMERICAL MODEL

For this study we implement the CFD-DEM algorithm to simulate a coupled particle-fluid system, which has been extensively employed to simulate systems where particle-fluid interactions are relevant (Tsuji *et al.*, 1993; Zhu *et al.*, 2007; Deen *et al.*, 2007; Zhu *et al.*, 2008; Zhao and Shan, 2013; Salikov *et al.*, 2015). The CFD component of the algorithm is solved using the Open Source package OpenFOAM while the DEM component is implemented using LIGGGHTS, which stands for LAMMPS Improved for General Granular and Granular Heat Transfer Simulations, and is an Open Source package for modelling granular material via the discrete element method (DEM). Coupling of the CFD and DEM components is facilitated by the Open Source coupling engine CFDEM which executes both the DEM solver and CFD solver consecutively. The CFDEM engine allows for execution of the program for a predefined number of time steps after which data is exchanged between the OpenFOAM solver and LIGGGHTS solver (Kloss *et al.*, 2012).

Discrete Element Method (DEM)

The discrete element method (DEM) is a soft contact model first introduced by Cundall and Strack (1979) to describe interactions between granular particles (Cundall and Strack, 1979). The simplest DEM contact model approximates grains as either disks in 2D or spheres in 3D, an approach that is sufficient to replicate laboratory-scale force chains (Aharonov and Sparks, 1999) and depict percolation-like contact networks (Fitzgerald *et al.*, 2014). Individual particles are tracked and their trajectories are numerically integrated over time and subject to local contact forces and torques, which develop when adjacent particles spatially overlap.

In this study we have adapted the DEM model to describe the interaction of spherocylinders with rotational and translational degrees of freedom. Consider spherocylinder i in a dense gas-fluidized reactor. The translational motion for spherocylinder i can be calculated by integrating

$$m_i \frac{d\mathbf{v}_i}{dt} = \mathbf{F}_{i,n} + \mathbf{F}_{i,t} + \mathbf{F}_{i,f} + \mathbf{F}_{i,p} + \mathbf{F}_{i,b} \tag{1}$$

where $\mathbf{F}_{i,n}$ is the total normal contact force acting on the particle, $\mathbf{F}_{i,t}$ is the total tangential contact force acting on the particle, $\mathbf{F}_{i,f}$ is the total hydrodynamic force acting on the particle (further details on these forces in the next section), $\mathbf{F}_{i,p}$ represents the pressure gradient acting on the particle and $\mathbf{F}_{i,b}$ is the total body force acting on the particle including gravity. The rotational motion of the particles can be solved using the expression

$$\mathbf{I}_i \frac{d\boldsymbol{\omega}_i}{dt} = \mathbf{T}_i \tag{2}$$

where $\mathbf{I}_i$ is the particle moment of inertia, $\boldsymbol{\omega}_i$ is the angular velocity of the particle and $\mathbf{T}_i$ is the net torque acting on the particle. Spherocylinder orientations are described by quaternions in the algorithm. For this study the equations of motion are integrated using the Velocity Verlet method.

In the case of spherical particles, particles overlap when the distance between the particle centres is less than the sum of the particle radii. For spherocylinder particles, the identification of contacts between particles, and the subsequent calculation of the overlap region, is more complicated than for spheres. Two adjacent spherocylinder particles are deemed to be overlapping once the distance between their shafts is smaller than the sum of their radii. Figure 1 shows an example of an overlapping contact between two spherocylinder particles P_1 and P_2. For particle P_i, R is the characteristic radius or radius of the spherical part of the spherocylinder, $\mathbf{r}_i$ is the centre of mass, L is the shaft length, $\mathbf{u}_i$ is the orientation unit vector originating at $\mathbf{r}_i$ and $\mathbf{v}_i$ is the translational

velocity. A spherocylinder contact detection algorithm originally developed for granular flows has been used in this study (Vega and Lago, 1994; Pournin *et al.*, 2005). For the sample contact illustrated in Figure 1 the shortest distance between the particles is given by $|\mathbf{s}_2 - \mathbf{s}_1|$, where $\mathbf{s}_1$ and $\mathbf{s}_2$ are points on the central axes of P_1 and P_2 respectively. The mid-point between the points $\mathbf{s}_1$ and $\mathbf{s}_2$ is $\mathbf{r}_c$ and the degree of overlap between the particles is expressed as δ_n. $\mathbf{n}_{12}$ and $\mathbf{t}_{12}$ are the normal and tangential unit vectors for the contact respectively.

To calculate the normal contact force exerted on particle P_1 by particle P_2 we use a linear spring-dashpot model such that the normal contact force is given by

$$\boldsymbol{F}_{12,n} = -k_n \delta_n \boldsymbol{n}_{12} - \eta_n \mathbf{v}_{12,n} \tag{3}$$

where k_n is the normal spring constant, η_n is the normal damping coefficient and $\mathbf{v}_{12,n}$ is the normal relative velocity between the particles. The tangential contact force is calculated from the Coulomb-type friction expression

$$\boldsymbol{F}_{12,t} = min(-k_t|\boldsymbol{\delta}_t|\boldsymbol{t}_{12} - \eta_t \mathbf{v}_{12,t}, -\mu|\boldsymbol{F}_{12,n}|\boldsymbol{t}_{12}). \tag{4}$$

In this expression k_t, $\boldsymbol{\delta}_t$, η_t, μ and $\mathbf{v}_{12,t}$ are the tangential spring constant, tangential overlap, tangential damping coefficient, friction coefficient and tangential relative velocity respectively. $\boldsymbol{\delta}_t$ is calculated from the time integral of the tangential relative velocity since the development of the initial particle contact and given by

$$\boldsymbol{\delta}_t = \int_{t_{c,0}}^{t} \mathbf{v}_{12,t} \Delta t \tag{5}$$

where $t_{c,0}$ is the time of initial contact between the particles. This expression represents the elastic tangential deformation of the particles since the onset of particle contact.

CFD

The fluid phase is described on basics of the volume-averaged Navier-Stokes equations which are discretized on a uniform grid. The equation of continuity is given by

$$\frac{\partial(\varepsilon_f \rho_f)}{\partial t} + \nabla \cdot (\varepsilon_f \rho_f \mathbf{v}_f) = 0 \tag{6}$$

where ε_f is fluid volume fraction, ρ_f is fluid density and $\mathbf{v}_f$ is the fluid velocity. The expression for momentum conservation is given by

$$\begin{aligned} \frac{\partial(\varepsilon_f \rho_f \mathbf{v}_f)}{\partial t} + \nabla \cdot (\varepsilon_f \rho_f \mathbf{v}_f \mathbf{v}_f) = \\ -\varepsilon_f \nabla p + \nabla \cdot (\varepsilon_f \boldsymbol{\tau}_f) + \mathbf{R}_{f,p} + \varepsilon_f \rho_f \mathbf{g} \end{aligned} \tag{7}$$

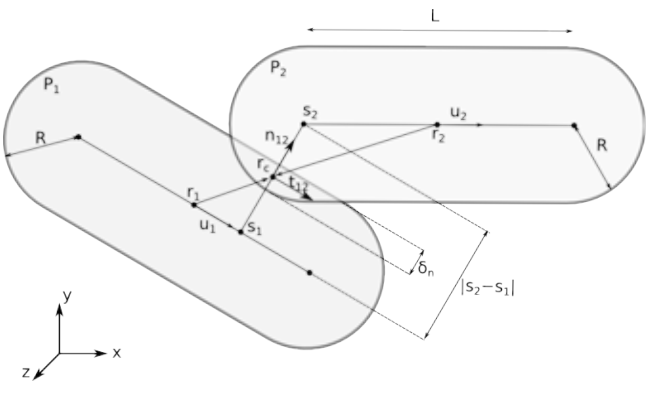

Figure 1: A schematic of a sample contact between two spherocylinders with each having a shaft length L and characteristic radius R.

where $\boldsymbol{\tau}_f$ is the stress tensor, $\mathbf{R}_{f,p}$ represents the momentum exchange between the fluid and particle phases and $\mathbf{g}$ is gravity.

Drag Force

The drag force on a single particle $\boldsymbol{F}_{D0}$ in a suspended flow in the absence of other particles acts in the direction of flow and is given by

$$\mathbf{F}_{D0} = \frac{1}{2} C_D \rho_f \varepsilon_f^2 \frac{\pi}{4} d_p^2 \left|\mathbf{v}_f - \mathbf{v}_i\right| (\mathbf{v}_f - \mathbf{v}_i) \tag{8}$$

where C_D is the drag coefficient, d_p is the particle volume equivalent diameter or the diameter of a sphere with the same volume as the spherocylinder, $\mathbf{v}_f$ is the gas velocity interpolated to the location of particle i, and $\mathbf{v_i}$ is the velocity of particle i. A precise expression for the drag force coefficient for spherocylinders is currently unavailable. However, a number of drag coefficients have been developed in the past that account for particle shape (Rosendahl, 2000; Loth, 2008; Hölzer and Sommerfeld, 2008; Zastawny *et al.*, 2012; Richter and Nikrityuk, 2013; Ouchene *et al.*, 2016). In this study, as an approximation, we employ the drag force correlation for arbitrary shaped particles established by Hölzer and Sommerfeld (Hölzer and Sommerfeld, 2008), which is given as

$$\begin{aligned} C_D = \frac{8}{\mathrm{Re}_p} \frac{1}{\sqrt{\Phi_\perp}} + \frac{16}{\mathrm{Re}_p} \frac{1}{\sqrt{\Phi}} + \frac{3}{\sqrt{\mathrm{Re}_p}} \frac{1}{\Phi^{3/4}} \\ +0.42 \times 10^{0.4(-\log \Phi)^{0.2}} \frac{1}{\Phi_\perp} \end{aligned} \tag{9}$$

where Re_p is the particle Reynolds number and for particle i is given as $\mathrm{Re}_p = \varepsilon_f \rho_f d_p \left|\mathbf{v}_f - \mathbf{v}_i\right| / \eta_f$ with η_f being the fluid viscosity, Φ is the particle sphericity and $\Phi_\perp$ is the crosswise sphericity. Besides being universally applicable to different shapes and easy to implement, this expression is accurate in that it has a mean relative deviation from experimental data of only 14.1%, significantly lower than previous expressions (Haider and Levenspiel, 1989; Ganser, 1993).

In a dense gas-fluidized system the drag force acting on a given particle will be affected by neighbouring particles. To account for this effect we implement a modified drag force expression (Felice, 1994)

$$\mathbf{F}_D = \frac{1}{2} C_D \rho_f \varepsilon_f^{1-\chi} \frac{\pi}{4} d_p^2 \left|\mathbf{v}_f - \mathbf{v}_i\right| (\mathbf{v}_f - \mathbf{v}_i) \tag{10}$$

where χ is a correction factor given by

$$\chi = 3.7 - 0.65 \exp\left[(-(1.5 - \log(\mathrm{Re}_p))^2/2\right]. \tag{11}$$

Lift Force

For non-spherical particles suspended in fluid flows a shape induced lift force on particles, similar to the concept of an aerofoil in aerodynamics, can significantly affect the trajectory of the particle. When the axis of elongated, rod-like or spherocylinder particle is inclined to the direction of fluid flow the flow fields on the upper and lower sides of the particle differ. The pressure drops in regions of rapid flow while the pressure increases in regions where the fluid velocity decreases (Richter and Nikrityuk, 2013), thus leading to an asymmetric pressure distribution and inducing a lift force perpendicular to the direction of fluid flow. An example of the lift force $\boldsymbol{F}_L$ due to a fluid flow for a spherocylinder that is not aligned with the direction of fluid flow is shown in

Figure 2. The lift force $\boldsymbol{F}_L$ does not align with the flow velocity, is orthogonal to $\mathbf{v}_{rel}$ and lies in the plane defined by the particle orientation vector $\mathbf{u}_i$ and $\mathbf{v}_{rel}$. For spherocylinder particles, there is no lift force when the central particle axis is aligned or perpendicular to the direction of fluid flow since there will be no resulting pressure difference. However arbitrary shaped particles can still be subject to a lift force even when they are aligned with the flow direction, similar to effects observed for a cambered airfoil.
The magnitude of the lift force F_L on a spherocylindrical particle is calculated from

$$F_L = \frac{1}{2} C_L \rho_f \varepsilon_f^2 \frac{\pi}{4} d_p^2 \left|\mathbf{v}_f - \mathbf{v}_i\right|^2 \tag{12}$$

where C_L is the lift force coefficient. To ensure that the lift force for a particle is orientated correctly, F_L is multiplied by the lift force orientation vector $\boldsymbol{F}_{Lo}$ which is given by

$$\boldsymbol{F}_{Lo} = \frac{\mathbf{u}_i \cdot \mathbf{v}_{rel}}{|\mathbf{u}_i \cdot \mathbf{v}_{rel}|} \frac{(\mathbf{u}_i \times \mathbf{v}_{rel}) \times \mathbf{v}_{rel}}{||(\mathbf{u}_i \times \mathbf{v}_{rel}) \times \mathbf{v}_{rel}||} \tag{13}$$

Thus the resultant lift force experienced by a particle is $\boldsymbol{F}_L = F_L \boldsymbol{F}_{Lo}$. Similar to drag force, the lift force exerted on a given particle can be influenced by other particles in proximity. In the absence of a proper correlation to account for the effect of surrounding particles on lift force, we have adapted the Di Felice correction originally intended for drag forces (Felice, 1994) and applied it to lift force such that the lift force F_L is given by

$$F_L = \frac{1}{2} C_L \rho_f \varepsilon_f^{1-\chi} \frac{\pi}{4} d_p^2 \left|\mathbf{v}_f - \mathbf{v}_i\right|^2. \tag{14}$$

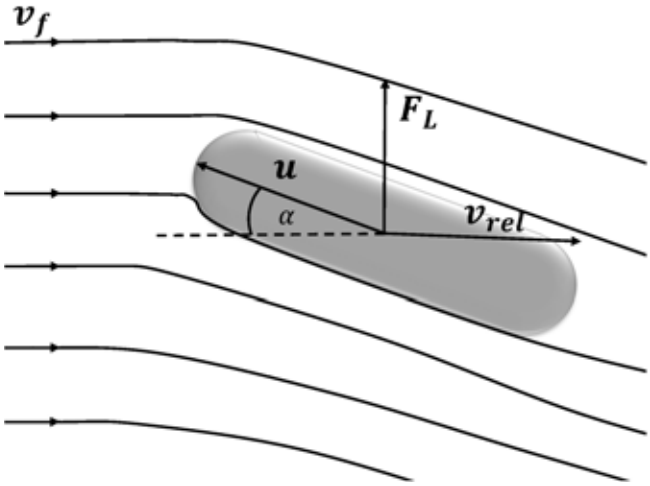

Figure 2: Lift vector orientation based on relative velocity $\mathbf{v}_{rel} = \mathbf{v}_f - \mathbf{v}_i$ and particle orientation vector $\mathbf{u}_i$. The angle of incidence of the fluid flow α is also indicated on the figure.

The lift force correlations considered in this study are presented in Table 1. In the expression from Hoerner, C_L is a function of the angle of incidence α and the drag coefficient C_D while particle shape and the flow characteristics are incorporated in the calculation of the drag coefficient (Hoerner, 1965). On the other hand, in the expression from Zastawny *et. al*, C_L is independent of C_D, and is dependent on Reynolds number and the angle of incidence while the shape of the particle is taken in to account with a number of fitting parameters b_1 to b_{10} (Zastawny *et al.*, 2012). These parameters can be estimated by fitting data from DNS simulations and have already been calculated for ellipsoids, disc-shaped particles and fibres with an aspect ratio of 5 (Zastawny *et al.*, 2012). Since these parameters are not applicable for the spherocylinders in this study, we use parameters for spherocylinders that have been fitted using in-house DNS simulations (Sanjeevi *et al.*, 2017). These parameters are presented in Table 2.

Table 1: Expressions for the lift correlations used in this study.

Authors	Correlation
Hoerner (1965)	$\frac{C_L}{C_D} = \sin^2\alpha\cos\alpha$
Zastawny *et. al* (2012)	$C_L = (\frac{b_1}{Re^{b_2}} + \frac{b_3}{Re^{b_4}}) \times \sin(\alpha)^{b_5 + b_6 Re^{b_7}} \times \cos(\alpha)^{b_8 + b_9 Re^{b_{10}}}$

Table 2: Values for the fit parameters for the Zastawny *et. al* (2012) lift coefficient expression specific for spherocylinder particles with an aspect ratio of 4.

Coefficient	Value	Coefficient	Value
b_1	1.884	b_6	0.003624
b_2	0.1324	b_7	0.6598
b_3	0.001668	b_8	-0.2621
b_4	-0.8159	b_9	0.8021
b_5	0.8562	b_{10}	0.04384

Simulation Parameters and Void Fraction

Table 3: Parameters for the CFD-DEM algorithm

CFD parameters	
Parameter	Value
Reactor dimensions	0.1 m × 0.1 m × 1.0 m
Number of cells	10 × 10 × 100
Minimum fluidisation velocity	$U_{mf} = 1.3$ m/s
Fluid velocity	$1.5U_{mf} = 1.95$ m/s
Time step (t_{CFD})	1 x 10^{-4} s
Fluid density (ρ_f)	1.2 kg/m^3
Spherocylinder & DEM parameters	
Parameter	Value
Number of particles	8000
Particle length	12 mm
Particle width	3 mm
Particle aspect ratio	4
Time step (t_{DEM})	1×10^{-5} s
Particle density (ρ_p)	1297 kg/m^3
Coefficient of friction (μ)	0.3
Initial bed height	0.1 m

Simulation parameters for the CFD-DEM algorithm are given in Table 3. The particle material properties represent those of the alumide particles used in previous experiments (Mahajan *et al.*, 2017). In addition, the dimensions of the fluidized bed reactor are equivalent to a laboratory scale apparatus. The fluid velocity is set such that we are operating in the bubbly regime, which was previously determined with experiments (Mahajan *et al.*, 2017). Simulation results correspond to a fluidization process over a laboratory timescale of 18 seconds, which is sufficiently long to ensure that the system has reached steady-state fluidization.

For this study we have defined a grid such that the length of each grid side is equal to approximately two diameters of the volume equivalent sphere, which in turn is equivalent to length of one spherocylindrical particle. For this preliminary investigation we have not explored the effect of grid size on the results presented. We anticipate that an increase in grid size will lead to changes in the drag and lift forces given the dependency of these forces on the void fraction (Equation 10 and Equation 12). Thus variation of the grid size will be examined in a future study.

Finally we present the approach used to calculate the fluid void fraction ε_f, which is required to solve the continuity equation (Equation 6) and the momentum conservation equation (Equation 7), in addition to calculating both the drag force (Equation 8) and lift force (Equation 12). To allow for the calculation of the solid fraction $(1-\varepsilon_f)$ contribution of any spherocylinder to the grid cells, the spherocylinder is assigned n_{sp} evenly spaced satellite points throughout its volume such that each satellite point carries an equal volume weight. First the parent cell for a particle is identified based upon the position vector $\mathbf{r}_i$ after which the particle volume is assigned to the parent cell and the neighbouring cells subject to the position of the satellite points. If the entire particle volume is contained within the parent cell then no distribution of particle volume is required. This approach for the calculation of ε_f in all cells can be optimised by varying n_{sp}.

RESULTS

We now present results from simulations subject to four different lift force conditions. In the first case we exclude lift forces such that particles are subject only to the drag force described by the Hölzer and Sommerfeld correlation with the Di Felice approximation that accounts for the effect of surrounding particles (Equation 10). In the second case, in addition to drag force, we include the lift force as described by the Hoerner correlation given in Table 1. In the third case, the lift force is described by the expression from Zastawny (Table 1) with the Di Felice approximation originally derived for drag force but adapted here for lift force (Equation 14). In the final case, we use the lift force expression from Zastawny without the Di Felice approximation (Equation 12).

A snapshot of a fluidized bed reactor subject to a fluid velocity of $1.5U_{mf}$ is shown in Figure 3(a). Boundaries are included along both the x-axis and y-axis. For all lift force cases, we present results pertaining to particle dynamics at three positions, $z = 0.075$ m, $z = 0.155$ m and $z = 0.245$ m, along the z-axis in the fluidized bed reactor as shown in Figure 3(b). The lowest z-position corresponds to a location close to the bottom of the reactor while the higher z-positions represent locations with more dilute particle conditions. All positions are midway along the y-axis as indicated in Figure 3(b). At each position we present analysis of the temporally averaged particle velocity in the direction of fluid flow (v_z), temporally-averaged void fraction measurements and temporally-averaged particle alignment with the z-direction along the x-axis. Thus we construct temporally averaged profiles along on the x-direction ($0.0\,\text{m} \geq \text{y} \geq 0.1\,\text{m}$) for a fixed z-position and fixed y-position, which is in the range $0.05\,\text{m} \geq \text{y} \geq 0.06\,\text{m}$. Typically a steady-state recirculation state is reached after approximately 5 s. Thus all temporal averages are calculated over the remaining simulation time, which is a period of approximately 13 s.

Particle Velocity

Figure 4 shows profiles of the temporally-averaged particle velocity parallel to the direction of the fluid flow along the x-axis $v_z(x)$ for the three analysis positions illustrated in Figure 3(b) and four lift force conditions. The value of v_z represents the temporal average of particles moving upwards and downwards in the reactor and can be used to study the resultant circulation pattern. The temporally-averaged particle velocity along the z-direction v_z at a given grid cell in the fluidized bed reactor over a specific time interval is calculated using the expression

$$v_z = \frac{\sum_{t=t_0}^{t_{\text{end}}} \sum_{p=1}^{N_{\text{cell}}(t)} v_z(p,t)}{\sum_{t=t_0}^{t_{\text{end}}} N_{\text{cell}}(t)} \tag{15}$$

where t_0 is the start time, t_{end} is the end time, $N_{\text{cell}}(t)$ is the number of particles in the grid cell at time t, p is the particle label and $v_z(p,t)$ is the velocity of particle p in the grid cell at time t.

Overall it can be seen that the inclusion of lift forces in the particle dynamics affects the form of $v_z(x)$. In general we find that the inclusion of any type of lift force leads to an overall increase in v_z. There are exceptions to this statement however. For example, at $x \approx 1$, without lift force, v_z is larger than all cases with lift force while at $z = 0.245$ m we find that a overall change in the form of v_z is only discernible for the case where the Zastawny lift force with the Di Felice approximation is used. The inability to resolve circulation patterns at the highest position is due to the fact that particle flow is quite dilute in this sector of the reactor. The larger value of v_z next to the wall in case without lift force is more likely due to the grid size rather than channeling effects. Given that we are operating above U_{mf}, a bubbling response will dominate over channeling, which is prominent just below U_{mf} (Mahajan *et al.*, 2017). We plan to explore the effect of grid size on the v_z profiles in a future study.

We also find that employing the Zastawany drag force expression with the Di Felice correction (Equation 14) leads to

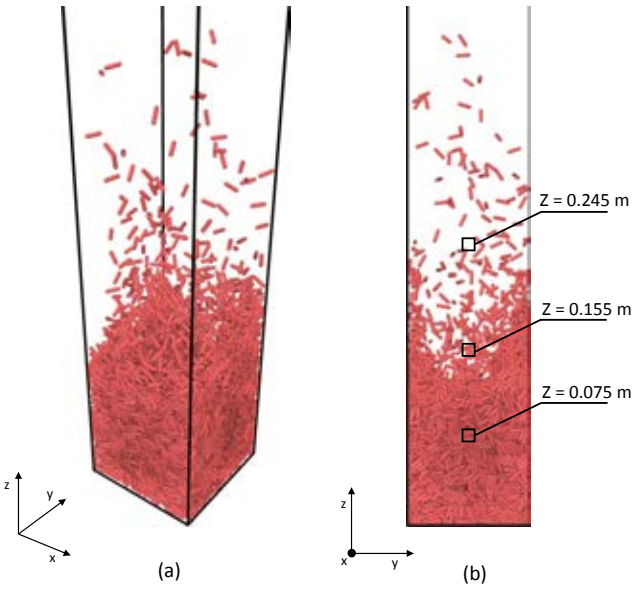

Figure 3: (a) Snapshot of the fluidized bed reactor with fluid velocity $1.5U_{mf}$. (b) Analysis positions in the bed reactor along the z-direction. These system snapshots were visualized using OVITO (Stukowski, 2010).

a much larger estimation of the lift force midway along the x-axis. In the case of results where the lift force is described by the Zastawany drag force without Di Felice (Equation 12), we resolve the average circulation pattern at $z = 0.075$ m where particles tend to rise on the left side of the reactor and fall on the right side of the reactor. Finally the velocity profiles for simulations using the Hoerner correlation are quite close to the case with no lift force, indicating that the Hoerner correlation has little or no effect on the velocity profiles.

Void Fraction

Figure 5 shows temporally-averaged void fraction profiles at the positions defined in Figure 3(b) for four lift force conditions. Variations in the void fraction reflect the trends observed in the v_z profiles presented in the previous section. The void fraction measure is linked to particle velocity as an increase in particle velocity can lead to increased dispersion of the particles in the reactor and hence an increase in void fraction at specific locations. For the case with the Zastawny lift force correlation with the Di Felice correction (Zastawny DF), we find an increase in the void fraction midway along the x-axis at $z = 0.075$ m and $z = 0.155$ m. This is similar to the increase observed in the v_z profiles. For the Zastawny lift force without the Di Felice correction (Zastawny), there is an obvious change in the recirculation pattern. Similar to the v_z profiles, void fraction profiles for the Hoerner correlation are analagous to the profiles for the case with no lift force. Finally at $z = 0.245$ m, the void fraction profiles for all lift forces cases are effectively indistinguishable with only minute variations in the profiles observed. In this domain of the reactor the particle flow is quite dilute and as a result, it is difficult to observe fluctuations in particle density.

Particle Orientation

The lift force crucially depends on particle orientation relative to the fluid and is a measure that certainly merits examination. Figure 6 shows temporally-averaged particle orientation profiles for the three analysis positions illustrated in Figure 3(b) and four lift force conditions. For this analysis we are only concerned with fluctuations in the z-component of the particle orientation and for each particle we calculate u_z^2 in order to scale the component between 0 and 1, thus avoiding negative orientation contributions. When a particle is perfectly aligned with the z-axis $u_z^2 = 1$. On the other hand, $u_z^2 = 0$ indicates that a particle is perpendicular to the z-axis or parallel to the xy-plane. A particle with $u_z^2 = 1/3$ is randomly orientated and does not preferentially align parallel or perpendicular to the z-axis. To emphasise the transi-

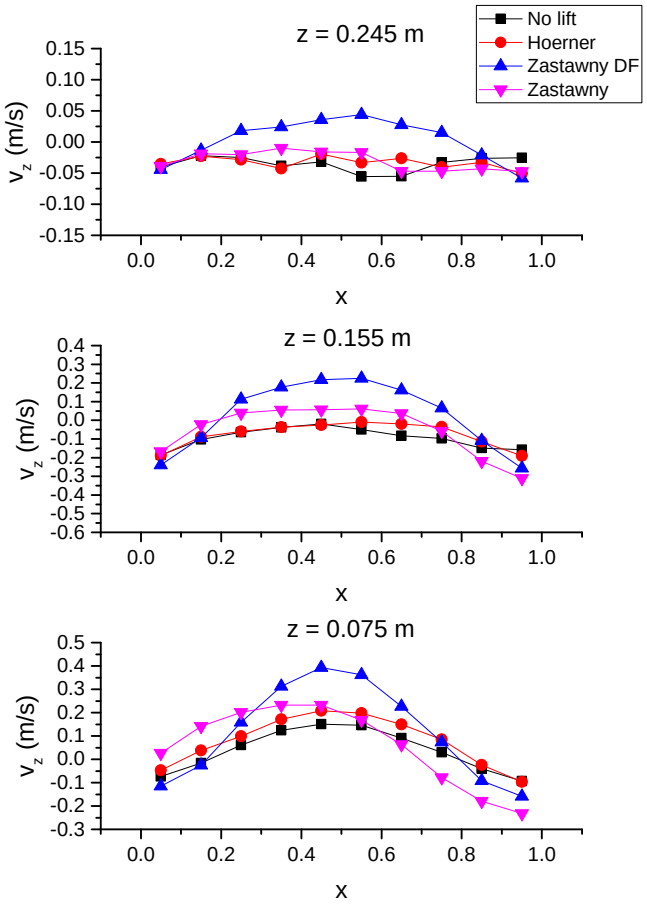

Figure 4: Comparison of the temporally-averaged v_z along the x-axis for the positions defined in Figure 3(b) in a fluidized bed reactor for the lift force cases: without lift force (No lift), lift force described by Hoerner correlation (Hoerner), lift force described by Zastawny correlation and Di Felice approximation (Zastawny DF) and lift force described by the Zastawny correlation (Zastawny). In these plots x is the position normalised by the length of reactor along the x-axis (0.1 m).

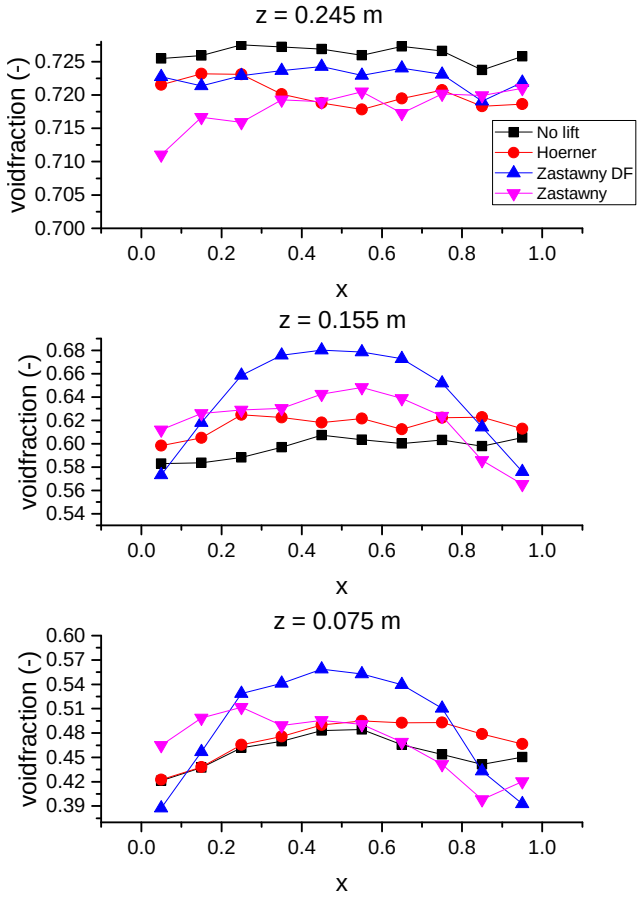

Figure 5: Comparison of the temporally-averaged void fraction along the x-axis for the positions defined in Figure 3(b) in a fluidized bed reactor for the lift force cases: without lift force (No lift), lift force described by Hoerner correlation (Hoerner), lift force described by Zastawny correlation and Di Felice approximation (Zastawny DF) and lift force described by the Zastawny correlation (Zastawny). In these plots x is the position normalised by the length of reactor along the x-axis (0.1 m).

tion in particle orientation that occurs at $u_z{}^2 = 1/3$, we study the variation of $u_z{}^2 - 1/3$ with x position such that a positive value is more aligned with the direction of flow or z-axis and a negative value indicates that particles are more aligned perpendicular to the flow.

From the profiles shown in Figure 6, boundary effects due to the walls are clearly visible in the profiles at $z = 0.075$ m and $z = 0.155$ m. At these positions particles tend to be more aligned with the z-axis close to the boundaries however contrasting behaviours are evident near the centre of the reactor. At $z = 0.075$ m, particles have a stronger tendency to align with the z-axis independent of the type of lift force. In contrast, at $z = 0.155$ m, particles have a much weaker tendency to align with the z-axis. In addition, at $z = 0.155$ m, for simulations with the Zastwany correlation (Zastawny), particles have a stronger inclination to align perpendicular with the z-axis while with the Zastawny correlation and Di Felice approximation (Zastawny DF) the orientation expression fluctuates around 0 at the centre of the reactor. At $z = 0.245$ m where the solid fraction is lowest, particles are randomly orientated with no discernible dependence on position relative to the rigid boundaries. Overall the results indicate that differing lift force cases do not affect particle orientation at bed positions studied here.

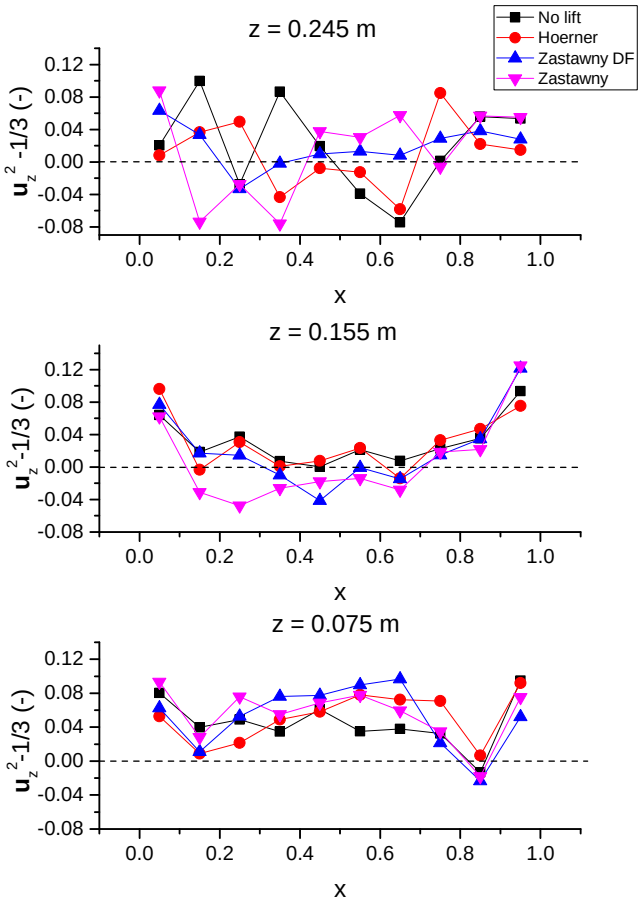

Figure 6: Comparison of the temporally-averaged z-component of particle orientation for the positions defined in Figure 3(b) in a fluidized bed reactor for the lift force cases: without lift force (No lift), lift force described by Hoerner correlation (Hoerner), lift force described by Zastawny correlation and Di Felice approximation (Zastawny DF) and lift force described by the Zastawny correlation (Zastawny). Each figure plots $u_z{}^2 - 1/3$ with x, where $u_z{}^2$ scales the component between 0 and 1 and $1/3$ is subtracted to allow for more intuitive comparison of the profiles. In these plots x is the position normalised by the length of reactor along the x-axis (0.1 m).

CONCLUSION AND OUTLOOK

We have investigated through simulation the relevance of lift forces on spherocylinder particles in dense gas-fluidized beds. To account for the coupling between the solid particle phase and fluid phase, we have implemented the CFD-DEM algorithm where the CFD component solves the fluid motion and the DEM component evaluates spherocylinder particle-particle interactions. The CFDEM engine, an Open Source software, has been used for program execution and coupling of the fluid and solid phases (Kloss *et al.*, 2012). Central to this study has been the implementation of a series of lift force closures in an attempt to establish the importance of lift forces on spherocylinder particle dynamics in a fluidized bed reactor. We have considered a lift force expression from aerofoil dynamics (Hoerner, 1965) and a lift force correlation derived for non-spherical particles of varying geometry (Zastawny *et al.*, 2012). In addition, we have accounted for the effect of neighbouring particles on the lift force experienced by a particle by combining the Di Felice condition (Felice, 1994) originally derived for drag forces with the Zastawny lift force correlation.

To quantify the effect of differing lift force expressions we have studied temporally-averaged particle velocity, void fraction and particle orientation at specific positions in a fluidized bed. Overall the results show that shape-induced lift force can have a considerable effect on the fluidization of spherocylinder or elongated particles with different lift force expressions predicting distinct responses. Using a lift force consisting of the Zastawny lift force correlation and the Di Felice neighbourhood approximation leads to a significantly higher values of the velocity along the z-axis (v_z) in comparison to the other lift force expressions (Figure 4). Trends in void fraction profiles have been shown to be comparable to those observed in the v_z profiles (Figure 5). For a given position in the reactor, an increase in particle velocity is suggestive of an increase in the local void fraction. Regions with low void fractions can also be indicative of increased particle interactions, leading to increased particle dissipation and therefore slower moving particles. However, during fluidization, clusters of co-aligned particles may develop in specific regions of the bed where the particles do not undergo appreciable dissipative interactions yet move faster than other similarly dense regions in the reactor. We plan on testing this proposal in a future study. Finally we examined particle orientation at different positions in the bed (Figure 6) where particles were found to align with the direction of flow near boundaries and in the middle of the bed near the fluid inflow region. However some distance above the base of the bed at $z = 0.245$ m where fewer particles are recorded as shown in Figure 3(b), particle orientation is effectively random with no preferred alignment of particles measured.

In this study we have demonstrated the relevance of lift force for the fluidization of spherocylinder particles in that the incorporation of a description of lift force clearly affects particle dynamics. As a result, we must identify conclusively the appropriate lift force expressions for spherocylinder particles that account for different particle aspect ratios and can be applied to flow conditions at high Reynolds numbers ($\mathrm{Re} < 2000$). This may involve further investigation with current expressions such as those developed specifically for ellipsoidal particles (Ouchene *et al.*, 2016) or the formula-

tion of expressions using DNS simulations. We will also explore the influence of grid size on the results presented in this study. In addition it may be necessary to develop more accurate drag force closures specific to spherocylinder particles. To gain a better insight into the fluidization response in real systems we will perform Magnetic Particle Tracking (MPT) experiments (Buist *et al.*, 2014) to compare results obtained experimentally with simulations subject to different lift force conditions. We also plan on implementing relevant torque expressions for the particles, studying larger systems, different particle aspect ratios and higher fluidization velocities.

ACKNOWLEDGEMENTS

The authors thank the European Research Council for its financial support under its consolidator grant scheme, contract no. 615906 (NonSphereFlow).

REFERENCES

AHARONOV, E. and SPARKS, D. (1999). "Rigidity phase transition in granular packings". *Phys. Rev. E*, **60**, 6890–6896.

ALAUDDIN, Z.A.B.Z., LAHIJANI, P., MOHAMMADI, M. and MOHAMED, A.R. (2010). "Gasification of lignocellulosic biomass in fluidized beds for renewable energy development: A review". *Renewable and Sustainable Energy Reviews*, **14(9)**, 2852 – 2862.

BRIDGWATER, A. (2003). "Renewable fuels and chemicals by thermal processing of biomass". *Chemical Engineering Journal*, **91(2-3)**, 87 – 102.

BRIDGWATER, T. (2006). "Biomass for energy". *Journal of the Science of Food and Agriculture*, **86(12)**, 1755–1768.

BUIST, K.A., VAN DER GAAG, A.C., DEEN, N.G. and KUIPERS, J.A.M. (2014). "Improved magnetic particle tracking technique in dense gas fluidized beds". *AIChE J.*, **60**, 3133–3142.

CUNDALL, P. and STRACK, O. (1979). "A discrete numerical model for granular assemblies". *Geotechnique*, **21**, 47 – 65.

DEEN, N., ANNALAND, M.V.S., DER HOEF, M.V. and KUIPERS, J. (2007). "Review of discrete particle modeling of fluidized beds". *Chem. Eng. Sci.*, **62(1-2)**, 28 – 44.

FELICE, R.D. (1994). "The voidage function for fluid-particle interaction systems". *International Journal of Multiphase Flow*, **20(1)**, 153 – 159.

FITZGERALD, B.W., CLANCY, I. and CORCORAN, D. (2014). "Bridging percolation and particle dynamics models of the granular rigidity transition". *Physica A: Statistical Mechanics and its Applications*, **410**, 582 – 594.

GANSER, G.H. (1993). "A rational approach to drag prediction of spherical and nonspherical particles". *Powder Technology*, **77(2)**, 143 – 152.

GIL, M., TERUEL, E. and ARAUZO, I. (2014). "Analysis of standard sieving method for milled biomass through image processing. effects of particle shape and size for poplar and corn stover". *Fuel*, **116**, 328 – 340.

GRACE, J.R., AVIDAN, A. and KNOWLTON, T. (1997). *Circulating Fluidized Beds*. Hoerner Fluid Dynamics.

HAIDER, A. and LEVENSPIEL, O. (1989). "Drag coefficient and terminal velocity of spherical and nonspherical particles". *Powder Technology*, **58(1)**, 63 – 70.

HOERNER, S.F. (1965). *Fluid-Dynamic Drag*. Hoerner Fluid Dynamics.

HÖLZER, A. and SOMMERFELD, M. (2008). "New simple correlation formula for the drag coefficient of non-spherical particles". *Powder Technology*, **184(3)**, 361 – 365.

HÖLZER, A. and SOMMERFELD, M. (2009). "Lattice boltzmann simulations to determine drag, lift and torque acting on non-spherical particles". *Computers and Fluids*, **38(3)**, 572 – 589.

KLOSS, C., GONIVA, C., HAGER, A., AMBERGER, S. and PIRKER, S. (2012). "Models, algorithms and validation for Open Source DEM and CFD-DEM". *Progress in Computational Fluid Dynamics*, **12(2/3)**, 140 – 152.

KRUGGEL-EMDEN, H. and VOLLMARI, K. (2016). "Flow-regime transitions in fluidized beds of non-spherical particles". *Particuology*, **29**, 1 – 15.

LOTH, E. (2008). "Drag of non-spherical solid particles of regular and irregular shape". *Powder Technology*, **182(3)**, 342 – 353.

MAHAJAN, V.V., NIJSSEN, T.M.J., FITZGERALD, B.W., HOFMAN, J., KUIPERS, H. and PADDING, J.T. (2017). "Fluidization of spherocylindrical particles". *Powders and Grains*.

MCKENDRY, P. (2002). "Energy production from biomass (part 3): gasification technologies". *Bioresource Technology*, **83(1)**, 55 – 63.

NIKOO, M.B. and MAHINPEY, N. (2008). "Simulation of biomass gasification in fluidized bed reactor using ASPEN PLUS". *Biomass and Bioenergy*, **32(12)**, 1245 – 1254.

OUCHENE, R., KHALIJ, M., TANIÈRE, A. and ARCEN, B. (2015). "Drag, lift and torque coefficients for ellipsoidal particles: From low to moderate particle reynolds numbers". *Computers and Fluids*, **113**, 53 – 64.

OUCHENE, R., KHALIJ, M., ARCEN, B. and TANIÈRE, A. (2016). "A new set of correlations of drag, lift and torque coefficients for non-spherical particles and large reynolds numbers". *Powder Technology*, **303**, 33 – 43.

POURNIN, L., WEBER, M., TSUKAHARA, M., FERREZ, J.A., RAMAIOLI, M. and LIEBLING, T.M. (2005). "Three-dimensional distinct element simulation of spherocylinder crystallization". *Granular Matter*, **7(2)**, 119–126.

RICHTER, A. and NIKRITYUK, P.A. (2013). "New correlations for heat and fluid flow past ellipsoidal and cubic particles at different angles of attack". *Powder Technology*, **249**, 463 – 474.

ROSENDAHL, L. (2000). "Using a multi-parameter particle shape description to predict the motion of non-spherical particle shapes in swirling flow". *Appl. Math. Modelling*, **24(1)**, 11 – 25.

SALIKOV, V., ANTONYUK, S., HEINRICH, S., SUTKAR, V.S., DEEN, N.G. and KUIPERS, J. (2015). "Characterization and CFD-DEM modelling of a prismatic spouted bed". *Powder Technology*, **270, Part B**, 622 – 636.

SANJEEVI, S., ZARGHAMI, A. and PADDING, J. (2017). "in preparation".

SON, S.R. and KIM, S.D. (2006). "Chemical-looping combustion with NiO and Fe_2O_3 in a thermobalance and circulating fluidized bed reactor with double loops". *Industrial & Engineering Chemistry Research*, **45(8)**, 2689–2696.

STUKOWSKI, A. (2010). "Visualization and analysis of atomistic simulation data with OVITO, the Open Visualization Tool". *Modelling and Simulation in Materials Science and Engineering*, **18(1)**, 015012.

TRAN-CONG, S., GAY, M. and MICHAELIDES, E.E. (2004). "Drag coefficients of irregularly shaped particles". *Powder Technology*, **139(1)**, 21 – 32.

TSUJI, Y., KAWAGUCHI, T. and TANAKA, T. (1993). "Discrete particle simulation of two-dimensional fluidized bed". *Powder Technology*, **77(1)**, 79 – 87.

VEGA, C. and LAGO, S. (1994). "A fast algorithm to

evaluate the shortest distance between rods". *Computers and Chemistry*, **18(1)**, 55 – 59.

WARNECKE, R. (2000). "Gasification of biomass: comparison of fixed bed and fluidized bed gasifier". *Biomass and Bioenergy*, **18(6)**, 489 – 497.

WERTHER, J. (2000). *Fluidized-Bed Reactors*, 320–366. Wiley-VCH Verlag.

WILLIAMS, P.T. and WILLIAMS, E.A. (1999). "Fluidised bed pyrolysis of low density polyethylene to produce petrochemical feedstock". *Journal of Analytical and Applied Pyrolysis*, **51(1-2)**, 107 – 126.

ZASTAWNY, M., MALLOUPPAS, G., ZHAO, F. and VAN WACHEM, B. (2012). "Derivation of drag and lift force and torque coefficients for non-spherical particles in flows". *International Journal of Multiphase Flow*, **39**, 227 – 239.

ZHAO, J. and SHAN, T. (2013). "Coupled CFD-DEM simulation of fluid-particle interaction in geomechanics". *Powder Technology*, **239**, 248 – 258.

ZHU, H., ZHOU, Z., YANG, R. and YU, A. (2007). "Discrete particle simulation of particulate systems: Theoretical developments". *Chemical Engineering Science*, **62(13)**, 3378 – 3396.

ZHU, H., ZHOU, Z., YANG, R. and YU, A. (2008). "Discrete particle simulation of particulate systems: A review of major applications and findings". *Chemical Engineering Science*, **63(23)**, 5728 – 5770.